MIT Libraries | DSpace@MIT

MIT Open Access Articles

Atomistic Simulation of a Thermoplastic Polyurethane and Micromechanical Modeling

Massachusetts Institute of Technology

Atomistic simulation of a thermoplastic polyurethane and micromechanical modeling

Nikolaos Lempesis[(1)], Pieter J. in 't Veld[(2)], Gregory C. Rutledge[(1)]

(1) Department of Chemical Engineering, Massachusetts Institute of Technology, 77 Massachusetts Avenue, Cambridge, Massachusetts 02139, United States

(2) BASF SE, GME/MM, Carl Bosch Str, 38, 67056 Ludwigshafen, Germany

ORCID iD's: Lempesis (0000-0002-4104-9666); in 't Veld (0000-0001-8460-5688); Rutledge (0000-0001-8137-1732)

Abstract: Thermoplastic polyurethanes constitute a versatile family of materials with a broad variety of engineering applications. However, connection between their chemical structure and mechanical properties remains elusive, in large part due to their heterogeneous nature, arising from segregation of chemically distinct segments into separate domains, with resulting complex morphologies. Using atomistic simulations, we examine the structure and mechanical properties of a common family of thermoplastic polyurethanes (TPU) comprising 4,4′-diphenylmethane diisocyanate and *n*-butanediol (hard segment) and polytetramethylene oxide (soft segment). A lamellar stack model previously developed for the study of semicrystalline polymers is applied here for the first time to a phase-segregated copolymer. Equilibrium structure and properties were evaluated for TPUs with different ratios of hard and soft components, using a combination of Monte Carlo and molecular dynamics simulations. Stress-strain behaviors were then evaluated using nonequilibrium molecular dynamics (NEMD) simulations. The compositional dependence of the Young's moduli thus obtained is shown to be well-approximated by a micromechanical homogenization model of the hard and soft components. Voigt (upper) and Reuss (lower) bounds of modulus were obtained for orientationally averaged aggregates, and shown to be greater than those measured experimentally. The discrepancy is explained in terms of the strain rate dependence of elastic moduli, characterized by an Eyring-like function.

For Table of Contents use only
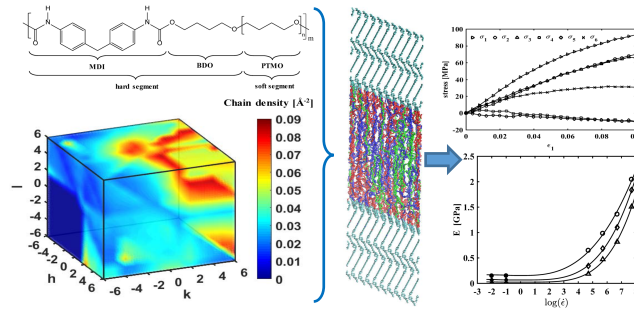
1. Introduction

The term "polyurethane" describes a diverse family of polymers produced by the polyaddition reaction of polyfunctional isocyanates, discovered in 1937 by Otto Bayer,[1] with compounds containing at least two hydroxyl groups. Polyurethanes span the spectrum of plastic, rubbery, and thermoset behaviors, depending upon their chemical constitution and morphology.[2] Thermoplastic polyurethanes (TPUs) are distinguished from the rubbers and thermosets by their linear structure, so that they can be melted and processed even after synthesis. They are typically formed by reacting together three chemical components: a di-isocyanate, a polyol, and a small diol known as the chain extender. The resulting polymer is a linear block copolymer of the polyol, called the soft segment, and short alternating sequences of di-isocyanate and chain extender, called the hard segment. Due to thermodynamic incompatibility, as well as steric and physicochemical properties of each of the components,[3] the hard and soft segments segregate into domains, called the hard component (HC) and the soft component (SC), respectively. The HC is characterized by highly ordered rod-shaped domains of about 5-20 nm interspersed at random orientations within an amorphous SC matrix.[4] TPUs are similar to thermoplastic semicrystalline polymers: at room temperature, the soft domains are amorphous and well above their glass transition temperature, $T_{g,SC} < T_{room}$, imparting the polyurethane with its extensibility, whereas the hard domains are below their melting (or vitrification) temperature, $T_{room} < T_{m,HC}$ $(T_{g,HC})$, endowing the polyurethane with mechanical stiffness.[5]

This heterogeneous, multi-block architecture of alternating crystalline or glassy domains and amorphous domains of different chemistry makes TPUs a remarkably versatile family of materials having a broad variety of engineering applications, including stimuli-responsive polymeric systems, self-healing composites, biodegradable materials, materials for additive manufacturing and bio-inspired robotics. Through suitable choice of constituent components, properties may be varied from those typical of soft elastomers to those of hard plastics, simply by alternating the dominant polyol from a flexible long-chain diol to a small molecule such as ethylene glycol.[6] Inspired by the astonishing mechanical properties of spider silk,[7, 8] in which superior extensibility and strength under tension arises from the copolymeric nature of the

polypeptide chains, materials scientists have developed TPUs with a variety of different block architectures, some of which are industrially scalable analogues of spider silk-like materials.[9]

Recently, polyureas were found to possess good dissipative properties, and were used as shock-mitigating materials.[10-12] The polyureas are very similar to TPU in their multi-block architecture and complex morphologies of hard and soft components. How the multi-block architecture of these materials enhances energy dissipation and shock mitigation hinges upon microstructure and constituent viscoelastic properties.[13] Tuning of viscoelastic properties of materials from purely viscous to purely elastic behavior can potentially enable a wide range of engineering applications including damping and noise reduction in automobile and aerospace industries,[14] conferring structural stability during wind and earthquake oscillations,[15] and mechanical damping.[16] The opportunity exists within TPUs to fine-tune the characteristics of different domains and their combination, maintaining, for example, high stiffness (high elastic modulus) while providing significant damping, i.e. relatively high loss modulus. The overarching goal is to design materials with tailored properties. The overall behavior of TPUs is very sensitive to the chemical and physical structures of the materials that are available to the synthetic chemist.

To address questions such as how different domains of HC and SC contribute to the macroscopically observed behavior of TPUs, we implemented a series of molecular simulations, with atomistic resolution. Molecular simulation is a powerful tool to gain detailed, mechanistic insight into the structure and response of complex polymeric materials. For the representation of the three dimensional structure of TPUs, we adopted the one dimensional lamellar stack motif. More complicated morphologies, such as dispersed or bicontinuous domains, may be envisioned to be built up by organizing appropriately the 1D lamellar stack in 3D space. The topology and packing of chain segments within the amorphous SC, sandwiched between two semi-infinite lamellar crystallites of the HC, was created by using the thermodynamically rigorous Interphase Monte Carlo (IMC) algorithm previously developed to study relatively simple semicrystalline hydrocarbons.[17-20] In this work, we combine and extend methods previously tested and used for the study of the individual constituents[21, 22] of TPUs with atomistic resolution, for the prediction of structural, thermodynamic, and mechanical properties of the copolymer system. Elsewhere, coarse-grained models of TPUs have been simulated using Dissipative Particle Dynamics to

evaluate the effects of hard and soft segment composition, block length and strength of interactions among these segments on extent of microphase separation and the resulting morphologies of TPUs.[23-25] The coarse-grained models were based on χ parameters estimated from atomistic simulations and experimental data.

This report is organized in the following way. In Section 2 a brief description is given of the models used to simulate TPUs based on knowledge gained from previous simulations of the HC and SC separately. We use these full TPU simulations to test a relatively simple method of micromechanical homogenization to approximate the stiffness matrices of TPUs of different composition, based on the stiffness matrices of the pure HC and SC. This approach is generalized from single body systems to polycrystalline materials by orientational averaging. A comparison to experimental measurements of elastic moduli for selected TPUs is provided in Section 3, and a strategy is reported to correct for the apparent strain rate dependence of elastic moduli. Lastly, Section 4 summarizes the basic findings of this work and discusses how they can be of use for future research.

2. Systems and methods

2.1 Force fields

In this work, the soft segment was poly(tetramethylene oxide) (PTMO), and the hard segment was 4,4′-diphenylmethane diisocyanate (MDI) with *n*-butanediol (BDO) as chain extender, henceforth denoted as MDI/BDO. The chemical structure of the TPU repeating unit is shown in Fig. 1. The TraPPE-UA force field was used for the soft segments, but modified with harmonic bond stretching potentials as described elsewhere.[21] This force field was previously shown to reproduce thermomechanical properties of the melt and crystal phases of PTMO individually, and to provide a reasonable description of elastic response of the semicrystalline PTMO interphase.[21] A force field based primarily on OPLS–UA[26-38] was used for the hard segments, but it was modified with Lennard-Jones interaction parameters (only) from TraPPE-UA.[39-44] This force field was also previously tested and validated in simulations for the structure and elastic properties of crystalline MDI/BDO.[22] Hydrogen bonds were not parameterized explicitly within the force field, but the packing of MDI/BDO segments in the HC were found to be consistent with geometrical criteria for hydrogen bond formation between the hydrogen and carbonyl oxygen of the urethane linkage.[45]
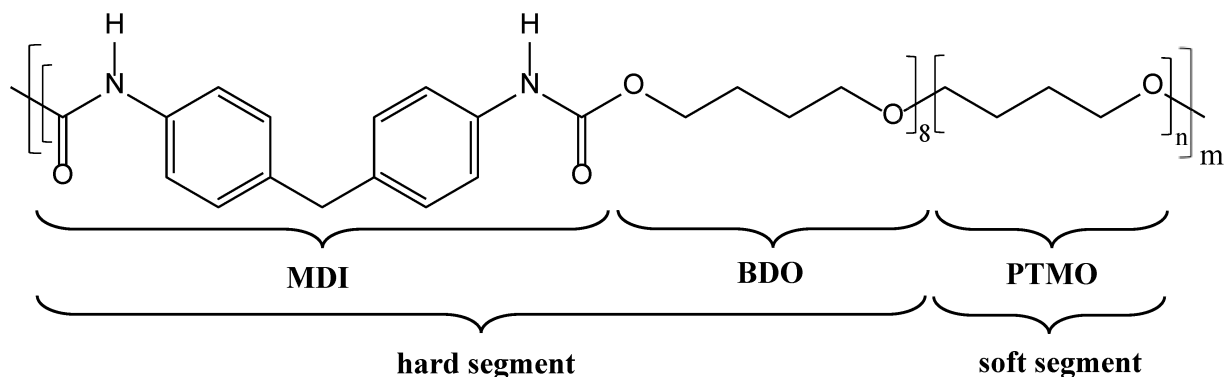
Figure 1. Chemical formula of the TPU repeat unit considered here.

2.2 Model Construction and Simulation

The Interphase Monte Carlo (IMC) algorithm, as implemented in the EMC software package,[19, 46] was used to create realistic atomistic configurations of the TPUs, in which both chemical connectivity (valence interactions) and intermolecular packing (steric and Coulombic interactions) can be maintained through the interface between the PTMO SC and the MDI/BDO HC. This method has been used extensively for the study of semicrystalline polyethylene,[17-19, 47, 48] polypropylene,[20, 49] and PTMO.[21] Analogously, TPUs are also semicrystalline to some extent, with the HC typically exhibiting a high degree of crystalline character, and the SC being mostly amorphous;[50, 51] in this work, the HC is modeled as crystalline MDI/BDO. The process followed in this work is illustrated schematically in Figure 2, and comprised several stages. In the first stage, we identified a facet of the MDI/BDO HC crystal that would serve well as the transition plane with the noncrystalline PTMO SC; this step is important because the distribution of loop and tail lengths in the noncrystalline domain have been found to depend on choice of crystal facet.[48] In the absence of any prior experimental or computational determination of the preferred crystal facet of the MDI/BDO crystal at the interface, we applied the chain flux method, which was reported previously to select the PTMO crystal facet that best matches the areal chain density of the amorphous PTMO melt ($d_w = 0.0453$ Å^{-2}) in semicrsytalline PTMO[21]. This method is based on the idea that the interfacial energy is lowest when the areal chain density (sometimes referred to as "chain flux"[52]) for the two abutting domains is the same. The results of the chain flux analysis for crystalline MDI/BDO are provided in the Supporting Information. From this

analysis, we determined that the low index crystal (001) facet, with an areal chain density $d_w =$ 0.049 Å^{-2}, is a suitable candidate. On this basis, semicrystalline TPU systems with the interfacial zone oriented parallel to the (001) crystallographic facet were selected for analysis in this work.

In the next step, we created a model of the perfect MDI/BDO crystal by replicating the MDI/BDO unit cell, reported previously by Lempesis et al,[22] N_a, N_b and N_c times in the a, b and c directions, respectively. The crystal MDI/BDO system was constructed so that the chain axis, which is parallel to the c-crystallographic axis of the triclinic MDI/BDO lattice,[22] was also parallel to the z-axis of the simulation box. For example, N_a=12, N_b=10 and N_c=7 resulted in a triclinic simulation box of total size 5.30 x 4.48 x 26.48 nm, containing 120 chains of 378 sites each, for a total of 45360 sites in the simulation box. The MDI/BDO segments were covalently bonded across the periodic boundary of the box in the z-direction.

In the third step, $N_m = N_c - 4$ layers of MDI/BDO unit cells in the z-direction were removed from the center of the simulation box, and the removed MDI/BDO segments were replaced with PTMO segments. Due to periodic boundary conditions in all 3 directions, the MDI/BDO layers at the top and bottom of the simulation box combined to form a semi-infinite crystal lamella 4 unit cells (~15.5 nm) thick, in accord with experimental X-ray diffraction and atomic force microscopy results for the hard domains of TPUs.[4, 53-57] Then, we inserted PTMO segments, each containing three repeat units per MDI/BDO repeat unit in the removed segments;[21] an integer number of repeat units was necessary to ensure that the PTMO chemistry was correct. Sites were placed in their crystallographic positions at the top and bottom (i.e. in the z-direction) of the simulation box.

In the fourth and final step, a fraction of the N_a x N_b chains were cut in the middle region of the simulation, a number of sites were removed from each chain, and 2 chain end sites were introduced to cap the segments of each chain where sites were excised. An NN$_e$VT Monte Carlo simulation (where N_e is the total number of chain end sites) was then performed with simulated annealing to equilibrate the noncrystalline SC, which results in amorphization of this domain away from the interface with the HC, while maintaining the chemical connectivity of soft segments with hard segments. Since the soft component of the TPUs was composed of PTMO segments, the amorphization process followed here was similar to the one used previously for the simulation of semicrystalline PTMO.[21] Both conventional and connectivity-altering Monte Carlo

moves were used, with precautions taken to ensure that the correct PTMO chemistry (i.e. –($C_\beta H_2 C_\alpha H_2 O C_\alpha H_2 C_\beta H_2$)–) was never compromised. As a result of the connectivity-altering moves and periodic boundary conditions, each simulation sampled from a distribution of multi-blocks of the form SS_t-[-HS-$SS_{l,b}$-]$_m$-HS-SS_t, $m=0,1,2,\ldots$, where 'SS' and 'HS' indicate PTMO soft segments and MDI/BDO hard segments, respectively, and the subscripts 't' and 'l,b' denote either a tail block or a loop or bridge block, respectively. The types of SS blocks connected to a single HS block are essentially uncorrelated, resulting in a statistical distribution of multi-blocks, as described elsewhere,[58] subject only to constraints imposed by the total number of tails, loops and bridges in the simulation. Both density and the orientational order parameter ($P_2 = \left(3\cos^2\theta_{jz} - 1\right)/2$) were calculated as functions of distance normal to the ab-plane in order to confirm that amorphization was achieved. In order to obtain the desired amorphous PTMO density at the midplane of the noncrystalline region, a total of 600 to 1200 sites were removed from the interphase region, in increments of 100 sites, in a series of NN_eVT Monte Carlo simulations. After removal of each increment, the system was re-equilibrated and the density at the midplane was calculated. A target value $\rho_a = 0.98$ g/cm^3 was used, based on the PTMO melt at 300 K.[21]
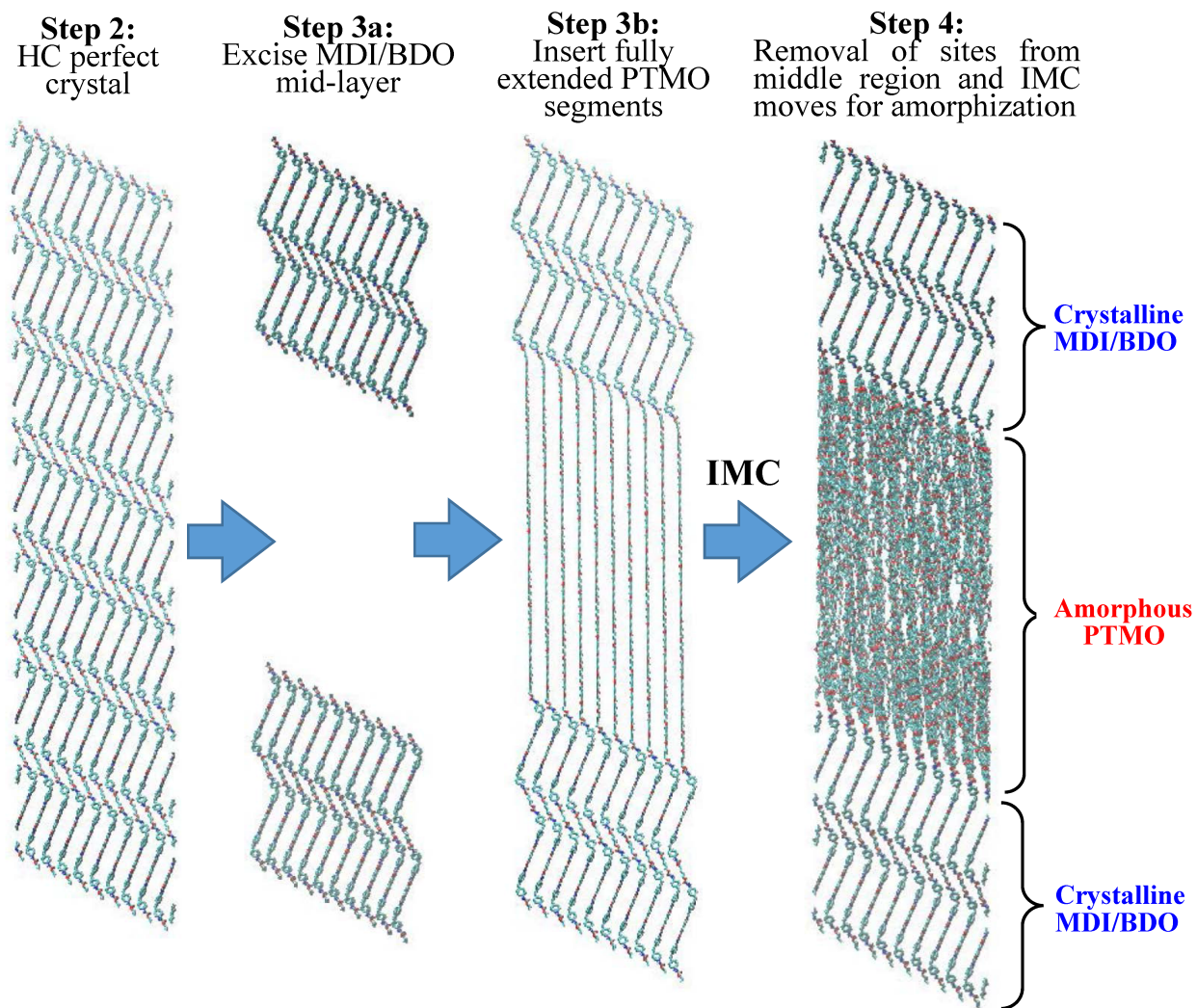
Figure 2: Schematic illustration of the four-step methodology used in this work for the creation of atomistic TPU configurations.

After completion of this 4-stage process to create realistic semicrystalline configurations of PTMO and MDI/BDO, an ensemble of 5 independent TPU configurations was transferred to LAMMPS,[59] and each was fully equilibrated in the NN_ePT ensemble for 20 ns, using Molecular Dynamics (MD) with a time step of 2 fs. The deterministic Nosé-Hoover thermostat and barostat were used to maintain isothermal and isobaric conditions[60, 61] with time constants (unless otherwise stated) of 100 and 1000 fs, respectively. The Velocity Verlet method[62] was used to integrate the equations of motion. After the completion of the MD simulations, the density profile along the direction normal to the ab-plane was calculated for each simulation and

averaged over the final densities of the five trajectories. Through that process, for example, we determined that the density in the amorphous area matched the target density for TPU68 when 600 sites were removed.

2.3 Morphological Analysis

Having thus constructed an atomistically detailed model of a TPU of a given composition, an ensemble of 10 completely independent initial configurations of that TPU, having the interfacial zone parallel to the (001) crystallographic plane, were created in like manner. To study the effect of composition, four different TPU ensembles were built and equilibrated. The concentration of HC/SC in all four TPU models was controlled by adjusting the values of N_a, N_b, N_c, N_m, N_r and N_e, keeping the amount of HC constant and equal to the average experimentally observed dimensions of four MDI/BDO unit cells (~15.5 nm). The characteristics of the four TPU model systems are summarized in Table 1.

Table 1: Details of the four TPU models simulated in this work. N_m is the number of MDI/BDO unit cells removed from each chain at stage 3 of the construction process. N_e is the number of resulting chain ends introduced, and N_r UAs were removed from the central noncrystalline PTMO region as part of the amorphization process ($2N_r/N_e$ UAs removed initially from each cut chain).

System name	HC [wt %]	Unit cells $(N_a \times N_b \times N_c)$	Dimensions [nm]	N_m	N_e, N_r
TPU68	68	(12 X 10 X 7)	5.30 X 4.48 X 26.48	3	60, 600
TPU55	55	(10 X 10 X 9)	4.42 X 4.86 X 30.86	5	56, 700
TPU43	43	(9 X 9 X 12)	4.02 X 4.49 X 39.45	8	40, 900
TPU30	30	(8 X 8 X 19)	4.22 X 4.56 X 46.00	15	32, 1200

2.4 Deformation Analysis

2.4.1 Non-equilibrium molecular dynamics (NEMD) simulations

The mechanical behavior of TPU68 was assessed by subjecting the 10 initial configurations to mechanical deformation. Prior to imposition of deformation, all configurations were equilibrated through MD simulations in the NσT ensemble for 10 ns each. This additional relaxation process ensured that all three principal elements of the stress tensor were equal to 1 atm, whereas all off-diagonal elements were zero. As in the case of equilibrium MD simulations (Section 2.2), the time step was 2 fs and the deterministic Nosé-Hoover thermostat and barostat were used to maintain isothermal and isobaric conditions throughout the NσT simulations, but with time constants of 100 fs for both. The components of the instantaneous stress tensor were calculated according to the method of Irving and Kirkwood.[63] For a more detailed description on how MD simulations were realized in the NσT ensemble, the reader is referred to Lempesis et al.[22] In the following, the Voigt notation[64] is used for stress and strain elements.

As was done previously for simulations of crystalline and semicrystalline PTMO,[21] three different loading protocols were considered. The first protocol implemented simple strain deformations using a non-steady-state, non-equilibrium form of MD in which the strain tensor had only one non-zero element, which evolved at a constant strain rate $\dot{\varepsilon} = 5 \times 10^6$ s^{-1}, up to a true strain of $\varepsilon = 0.1$, while the other components were held constant at their undeformed values. Through that process 36 stress-strain plots were obtained. All 36 components of the full elastic stiffness tensor $\mathbf{C}$ of each TPU composition were calculated from the slopes of these plots up to a true strain of 2%.[65, 66] The elastic compliance tensor was then calculated as the inverse of the stiffness tensor $\mathbf{S} = \mathbf{C}^{-1}$. The inverses of the diagonal elements of the compliance tensor are equal to the elastic moduli of the material:[67] Young's moduli $E_i = 1/S_{ii}$, $i=1,2,3$ and shear moduli $G_{i-3,} = 1/S_{ii}$, $i=4,5,6$. The isothermal compressibility and the bulk modulus were calculated from the components of the stiffness tensor elements using $\beta_T = [S_{11} + S_{22} + S_{33} + 3(S_{12} + S_{23} + S_{13})]$ and $K = \beta_T^{-1}$, respectively.

In the second loading protocol, called "uniaxial extension", the system was elongated uniaxially in one of the three principal directions (x,y,z), while maintaining zero stress in all of the other directions, allowing thus the lateral dimensions to change freely according to the Poisson ratio of the material in these directions. This type of loading yielded independent estimates of the Young's moduli E_i, and isothermal compressibility β_T. The third loading protocol, called "bulk compression", consisted of a small compressive strain imposed in all three

principal directions simultaneously in a very short NEMD simulation. By tracking the change in pressure as a function of strain, the isothermal compressibility of the material was calculated directly. The two last types of deformation served as checks on the numerical accuracy of the first deformation protocol (simple strain), which is itself complete.

2.4.2 Micromechanical homogenization

A micromechanical homogenization technique called the "composite inclusion model" (CIM) was used to determine to what extent a full TPU simulation was required to get accurate estimates of their elastic properties. This method was developed by Ahzi et al.,[68, 69] and allows one to compute the elastic stiffness tensor for a layered composite, given the volume fractions and stiffness tensors for the component layers, in this case the MDI/BDO crystal and a semicrystalline PTMO. This method represents a compromise between the Voigt and Reuss mixture formulae by introducing strain and stress concentration tensors that act as weight functions. The weight functions are determined through the simultaneous enforcement of the conditions for continuity of deformation and traction equilibrium at the interface between the component layers. Extended CIM (ECIM) extends CIM from bi-layer to tri-layer systems, and was originally used in the reverse direction, as a dissociating tool to extract the stiffness tensor of the interfacial layers in semicrystalline polyethylene from the stiffness tensor of the entire noncrystalline domain, comprising two interfaces and the purely amorphous domain.[70, 71]

In this work, CIM was used in the forward direction to estimate the elasticity of a TPU based on the elasticities of its relatively simpler constituent parts: a layer of semicrystalline PTMO[21] and a layer of crystalline MDI/BDO.[22] In the TPU system of Figure 2, the outermost layers are both crystalline MDI/BDO; due to periodic boundary conditions imposed in our model, those two layers may be treated as part of the same layer. Although, there are various other micromechanical homogenization techniques in the literature, such as the double-inclusion method (DIM) developed by Hori and Nemat-Nasser,[72] CIM has the advantage that no Eshelby tensor or random reference medium is needed, resulting in fewer independent variables that need to be determined.

The elasticity $\mathbf{C}^{\mathrm{CIM}}$ of the composite is described by the following equation:

$$\mathbf{C}^{\text{CIM}} = \eta_{\text{HC}} \mathbf{C}^{\text{HC}} \mathbf{Q}^{\text{HC}} + \eta_{\text{SC}} \mathbf{C}^{\text{SC}} \mathbf{Q}^{\text{SC}} \tag{1}$$

Superscripts on all tensors of Eq. 1 (**C** and **Q**), refer to the component of the composite. By virtue of Eq. 1, CIM predicts that the mechanical behavior of the composite system, $\mathbf{C}^{\text{CIM}}$, is a linear combination of two contributions; one coming from crystalline MDI/BDO (expressed by $\mathbf{C}^{\text{HC}}$) and the second one from semicrystalline PTMO (expressed by $\mathbf{C}^{\text{SC}}$), weighted by the volume fractions of these two components, η_{HC} and η_{SC} respectively, and the corresponding strain concentration matrices **Q**. The strain concentration matrices **Q** are 6x6 matrices whose elements are calculated using the following three equations:[69]

$$\mathbf{Q}^{i}_{\alpha j} = \boldsymbol{\delta}_{\alpha j} \tag{2}$$

$$\mathbf{Q}^{\text{HC}}_{\beta j} = \left[\mathbf{C}^{\text{HC}}_{\beta\beta'} + \frac{1 - \eta_{\text{SC}}}{\eta_{\text{SC}}} \mathbf{C}^{\text{SC}}_{\beta\beta'} \right]^{-1} \left[\frac{1}{\eta_{\text{SC}}} \mathbf{C}^{\text{SC}}_{\beta\beta'} \boldsymbol{\delta}_{\beta j} - \left(\mathbf{C}^{\text{HC}}_{\beta\alpha'} + \frac{1 - \eta_{\text{SC}}}{\eta_{\text{SC}}} \mathbf{C}^{\text{SC}}_{\beta\alpha'} \right) \boldsymbol{\delta}_{\alpha j} \right] \tag{3}$$

$$\mathbf{Q}^{\text{SC}}_{\beta j} = \frac{1}{\eta_{\text{SC}}} \left(\boldsymbol{\delta}_{\beta j} + \left(1 - \eta_{\text{SC}} \right) \mathbf{Q}^{\text{HC}}_{\beta j} \right) \tag{4}$$

The indices in the above set of equations are as follows:

$i = \{ \text{HC}, \text{SC} \}$, $j = [1,6]$ and $\alpha, \alpha' = 1,2,6$ and $\beta, \beta' = 3,4,5$

2.4.3 *Orientationally averaged aggregates*

The relation between the elastic properties of individual anisotropic bodies, such as the one depicted in Figure 2, and aggregates comprising a large number of such bodies arranged according to a prescribed orientation distribution function has been described in texts like that of Arridge[65] under the assumption of either uniform strain (Voigt average[73]) or uniform stress (Reuss average[74]). Hill showed theoretically that the Voigt moduli represent upper bounds, and the Reuss moduli lower bounds, on the true moduli of the aggregate.[75] For the special case of random distribution of orientation, assumed here, the calculation of the Voigt bound of the orientationally averaged elastic moduli simplifies to the following set of equations:

$$E_V = \frac{(A - B + 3C) \cdot (A + 2B)}{2A + 3B + C} \tag{5}$$

$$G_V = \frac{(A - B + 3C)}{5} \tag{6}$$

where A = C_{11} + C_{22} + C_{33}, 3B = C_{23} + C_{31} + C_{12}, and 3C = C_{44} + C_{55} + C_{66} . Similarly, for the Reuss bound under the assumption of random orientation distribution, the calculation simplifies to:

$$\frac{1}{E_R} = \frac{1}{5}(3A' + 2B' + C') \tag{7}$$

$$\frac{1}{G_R} = \frac{1}{5}(4A' - 4B' + 3C') \tag{8}$$

where 3A′ = S_{11} + S_{22} + S_{33}, 3B′ = S_{23} + S_{31} + S_{12}, and 3C′ = S_{44} + S_{55} + S_{66}

2.4.4   Rate dependence of elastic moduli

To quantify the impact of deformation rate on the elastic moduli of TPUs, additional NEMD simulations were conducted for semicrystalline PTMO and crystalline MDI/BDO. In addition to the results obtained for these systems in previous studies at $\dot{\varepsilon}_i$ = 5 x 10^6 s^{-1}, their mechanical response was studied at three additional deformation rates, $\dot{\varepsilon}_i$ = 5 x 10^7 s^{-1}, 5 x 10^5 s^{-1}, and 5 x 10^4 s^{-1}, up to a true strain of ε_i = 0.03.

The CIM homogenization method (Section 2.4.2) was applied to the pure component stiffness matrices obtained by NEMD at each deformation rate, to obtain estimates of the composite stiffness matrices for the four TPU compositions at each deformation rate. Then, orientational averages (Section 2.4.3) were calculated for all four TPU systems at each of the four deformation rates, and the corresponding Voigt and Reuss limits for Young's and shear moduli were calculated with the help of Eqs. 5-8.

The strain rate dependences of yield stress[76, 77] and elastic moduli[78, 79] for various polymer systems have been described effectively using an Eyring-like hyperbolic sine function.

After orientational averaging the results of NEMD simulations at the different strain rates were fitted using Eq. 9:

$$E(\dot{\varepsilon}) = K + L\sinh^{-1}(M\dot{\varepsilon})^P \tag{9}$$

Here, K is a material parameter that describes the athermal internal yield stress, and L = $2KT/V_{act}$, where V_{act} is the activation volume. $M = \dot{\varepsilon}_0 \exp(\Delta H_i/RT)$, where $\dot{\varepsilon}_0$ is a constant pre-exponential strain rate parameter and ΔH_i describes the activation energy of the process responsible for strain rate softening. Finally, P=1/n, where n is a material parameter used to characterize the cooperative movement of chain segments. In this work, the parameters K, L, M, and P in Eq. 9 are fitting parameters.

3. Results and Discussion

During the course of the MD simulations, the density of the system and the orientational order parameter were monitored. Each equilibration simulation ran for a total of 20 ns, the last 15 ns of which were sampled every 500 fs to calculate ensemble averages. The average density and P_2 profiles for the system with N_a=12, N_b=10 and N_c=7 (TPU68), averaged over the 10 trajectories, are shown in Figure 3(a) and 3(b), respectively; density and P_2 profiles for the other systems were similar, and are included in the Supporting Information. Both order profiles confirm the presence of crystal and amorphous domains. The difference in density between the crystalline and noncrystalline domains, in addition to the transition zone separating them, is readily apparent. For reasons of clarity, error bars have been omitted from all simulation points of Figure 3; the standard error for density at each *d*-value was less than 2% of the mean in all cases.
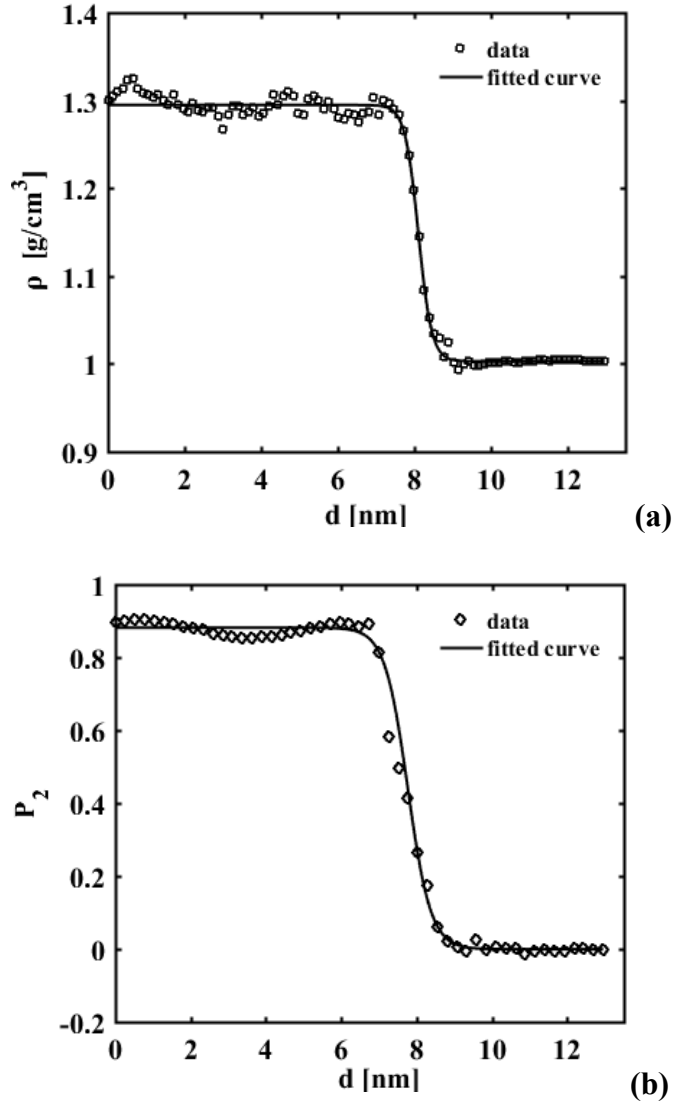
Figure 3: Average order parameter profiles of equilibrated TPU68 as functions of distance d normal to the ab-plane: (a) density profile $\rho(d)$; (b) orientational order profile $P_2(d)$. In both parts, the hyperbolic tangent function (solid curve) is a nonlinear least squares fit to the simulation data (open symbols). The simulation results have been mirrored across the center plane of the simulation box for purposes of computing the average profiles.

The calculated average density of the crystalline region was $\rho_c^{sim} = 1.30 \pm 0.02$ g/cm^3, very close to the experimentally measured[80, 81] crystalline MDI/BDO density $\rho_c^{exp} = 1.31 \pm 0.01$ g/cm^3. The uncertainty in the experimental density reflects the deviation in values reported by

different research groups. Similarly, the average computed density for the amorphous region, $\rho_a^{sim} = 1.00 \pm 0.01$ g/cm^3 compares favorably to the target melt PTMO density[21, 82] extrapolated to room temperature, $\rho_a = 1.00 \pm 0.02$ g/cm^3. Agreement is generally quite good, confirming the validity of the selected force field to describe inter- and intramolecular interactions realistically both for the crystalline MDI/BDO and the amorphous PTMO domains. Figure 3(b) shows the P_2 profile as a function of distance d normal to the ab-plane for the TPU68 system. The shape of the P_2 profile is characteristic of a transition from a highly ordered crystalline domain (high P_2 values) to a disordered, completely amorphous domain ($P_2 = 0$). In both order profiles of Figure 3, a hyperbolic tangent function $f(d) = H + (H - h)\tanh[\lambda(d - \zeta)]$ was used to fit the simulation points, where f is the order parameter (ρ or P_2), H is the asymptotic value of the order parameter for the crystalline phase, h is the asymptotic value of the order parameter for the amorphous phase, $1/\lambda$ is a measure of the interfacial width separating crystalline and amorphous domains, and ζ is the inflection point.[83]

The thickness of the interphase between hard and soft components was extracted separately from both the density and the P_2 profiles, with the help of the corresponding fitting parameters λ, averaged over the 10 TPU configurations, and plotted as a function of composition in Figure 4. The interphase thickness appears to be about 1.4 nm, independent of composition; this value is very similar to the average interfacial thickness calculated for semicrystalline polyethylene[17, 84, 85] (~ 1.0 nm) and semicrystalline PTMO[21] (~ 1.2 nm).
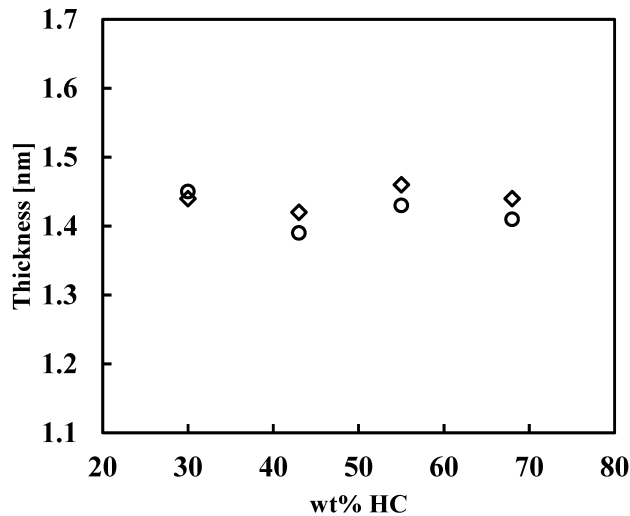
Figure 4: Average interfacial thickness as a function of HC content in TPUs extracted from density (open circles) and P_2 profiles (open rhombuses).

The probability distributions of tails, loops and bridges in the noncrystalline region of TPU68 as functions of their number of constituent united atoms, N_b, are shown in Figure 5. It has been previously seen that for $N_b > 100$, these distributions decay exponentially, indicative of a most probable distribution of segment lengths, as defined by Krishna Pant et al.[86] Additionally, internal equilibration between the populations of loops and bridges is confirmed by their overlap for $N_b > 100$. The Boltzmann probability associated with the existence of a soft segment of length N_b is proportional to $\exp(\beta\mu_{bead}N_b)$, where μ_{bead} is the incremental chemical potential required for the insertion or removal of a single UA.[20]

From the slopes of the probability distributions of Figure 5 in semilog format, incremental chemical potentials μ_{bead} for all three types of topological features (loops, bridges, and tails) were calculated to be -0.026 ± 0.0016, -0.024 ± 0.0026, and -0.031 ± 0.0021 kJ/mol, respectively. Although there are no experimental measurements available in the literature for the chemical potential required to insert or remove a PTMO bead in the noncrystalline domain of a TPU, nevertheless, the calculated values of this work are very similar to their counterparts computed for semicrystalline PTMO[21] and isotactic polypropylene.[20] The minimum number of beads $N_{b,min}$ in all three populations is consistent with the observations and length constraints reported for semicrystalline PTMO.[21] More precisely, the shortest observed bridge for TPU68 was 102 beads, slightly larger than the minimum number of beads (95) required to span the noncrystalline region with a fully extended, all trans conformation. Short loops appear to be slightly more likely than short tails. We hypothesize that the small difference between the population distributions of loops and tails at small N_b arises due to better packing of short loops than short tails within the relatively higher density region of the interface. The average number of blocks per chain ($2\langle m\rangle+3$) was found to be 4.32 ± 0.14.
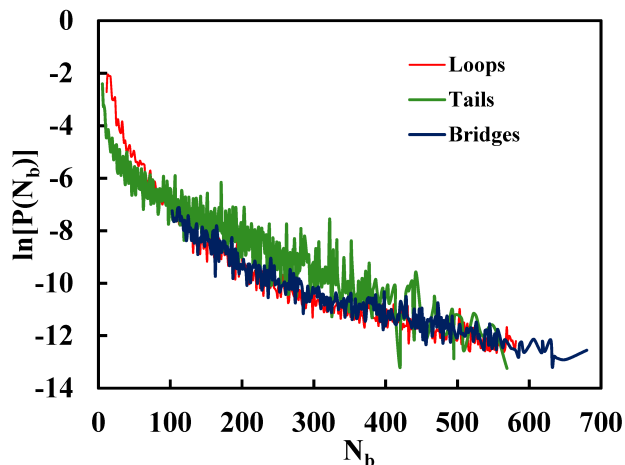
Figure 5: Probability distribution of loops, tails, and bridges in the noncrystalline region of TPU68 as function of segment length.

Figure 6 shows a representative set of 6 stress-strain curves, averaged over 10 trajectories, resulting from the NEMD simulations of simple strain deformation of TPU68 at the strain rate $\dot{\varepsilon}_1 = 5 \times 10^6$ s^{-1}. Similar plots were generated for the other 5 simple strain deformations; these plots are provided in the Supporting Information. For reasons of clarity, error bars have been omitted from Figure 6; the standard error in all cases is on the order of 5 MPa. From linear fits to the slopes of these curves (and the ones provided in the Supporting Information) up to 2% strain, all 36 elements of the stiffness tensor **C** were calculated.

A number of interesting observations can be derived from the stress-strain behaviors shown in Figure 6. At low strains (<2%), all of the stress-strain plots have finite slope, which is indicative of 36 nonzero stiffnesses. The symmetry of the simulation cell is determined by the component of lowest symmetry within it; given the triclinic symmetry of the crystalline MDI/BDO unit cell,[22] 21 of these 36 stiffnesses should be independent. Indeed, the stiffness matrix was confirmed to be approximately symmetric about its main diagonal; in what follows, advantage has been taken of this symmetry to average the upper and lower triangular elements of the stiffness matrix, and only the upper triangular values are reported. All stiffness matrices were confirmed to be positive definite, a necessary condition for mechanical stability. Additionally, at low strains ($0 < \varepsilon_i < 0.02$), the response was approximately linear and elastic, as

confirmed by relaxation of stresses upon reversal of strains (not shown). Equation 10 shows the calculated stiffness matrix in GPa for TPU68 obtained at $\dot{\varepsilon}_i = 5 \times 10^6 \text{ s}^{-1}$.

The elastic Young's, shear and bulk moduli for TPU68 are provided in Table 3, where applicable, based on the deformation protocol (*c.f.* Section 2.4.1) used for their estimation. Table 3 confirms that elastic constants calculated by the three different loading conditions are consistent. It also shows the anisotropic nature of TPU68, imparted by the anisotropic crystalline MDI/BDO component. The calculated mechanical response of TPU68 is intermediate to that of crystalline MDI/BDO and semicrystalline PTMO, reported previously.[21, 22] When deformed in the z- (or 3-) direction ($\sigma_i - \varepsilon_3$, $i = [1,6]$), the response of TPU68 ($E_3 = 0.63$ GPa) is similar to the corresponding stress-strain response of semicrystalline PTMO ($E_3 = 0.32$ GPa) when deformed in the same direction, confirming that deformation normal to the interface in this layered system is dominated by the softer semicrystalline PTMO component, as expected for a composite deformed in series. When deformed parallel to the interface in this layered system (ε_1 and ε_2) the response of TPU68 is dominated by the stiffer crystalline MDI/BDO domains, as evidenced by E_1 and E_2 values closer to those of crystalline MDI/BDO. Similarly, when deformed in shear (G_1, G_2), TPU68 is closer to the corresponding values of semicrystalline PTMO when the shear gradient is perpendicular to the interface, but the shear modulus G_3 lies closer to the value of crystalline MDI/BDO when the shear gradient is parallel to the interface.

At intermediate strains ($0.02 < \varepsilon_i < 0.1$), a transition from linear-elastic to nonlinear behavior takes place. Within this strain interval, rather than a sharp yield point, a stress rollover was observed in most cases, indicative of a gradual strain-induced softening.
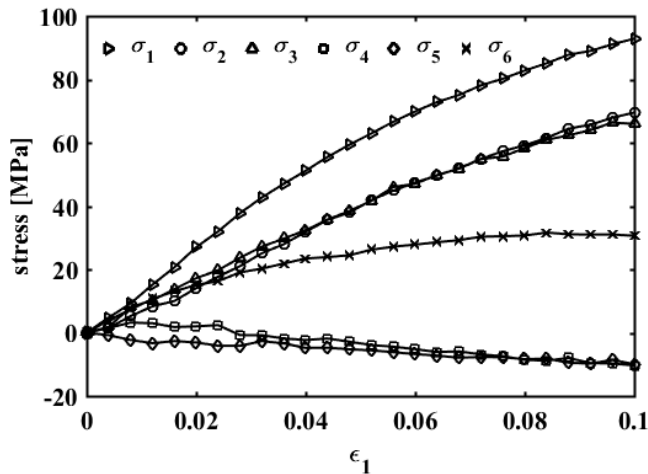
Figure 6: Linear-elastic true stress - true strain behavior of TPU68 under simple straining (extensional along ε_1) at $T = 300$ K and $P = 1$ atm. The slopes of these plots, up to a true strain of 2% were used to evaluate the corresponding elements of the stiffness matrix. (For the remaining extensional and shear deformation plots, the reader is referred to the Supporting Information).

$$C_{\text{TPU68}} = \begin{bmatrix} 1.83 & 0.96 & 1.20 & -0.04 & -0.26 & 0.16 \\ & 2.21 & 0.82 & -0.08 & -0.14 & -0.30 \\ & & 1.78 & 0.30 & -0.18 & 0.31 \\ & & & 0.65 & -0.49 & 0.15 \\ & & & & 0.90 & -0.21 \\ & & & & & 1.26 \end{bmatrix} \tag{10}$$

Table 3: Linear elastic properties calculated via NEMD for TPU68 at $T = 300$ K and $P = 1$ atm. Uncertainty in all elastic moduli is of the order of 0.05 GPa.

TPU68			
Def. Method	**simple strain**	**uniaxial strain**	**isotropic compression**
Property			
E_1, E_2, E_3 **[GPa]**	0.70, 1.45, 0.63	0.76, 1.40, 0.66	N/A
G_1, G_2, G_3 **[GPa]**	0.25, 0.39, 1.05	N/A	N/A
K **[GPa]**	1.26	1.22	1.20

Next, the complete elastic stiffness tensor was estimated as a function of TPU composition, based on the pure component stiffness tensors for crystalline MDI/BDO and semicrsytalline PTMO, using the CIM method as described in Section 2.4.2. The results of the CIM approach are compared to the NEMD results for stiffness, to check the accuracy of the CIM approximation for the TPUs. The stiffness matrices $\mathbf{C}^{HC}$ and $\mathbf{C}^{SC}$, for crystalline MDI/BDO and semicrystalline PTMO respectively, were taken from previous studies.[21, 22] The strain concentration matrices were calculated with the help of Eqs. 2-4. The volume fraction of HC for all TPU concentrations was estimated by a linear fit to the volume fractions of the four TPU systems considered here and the two extreme cases of 0 wt % HC and 100 wt % HC; small

differences in the contribution of interfacial density make this trend different from simple parity. The trend is shown in Figure 7. The equation $\eta_{HC} + \eta_{SC} = 1$ was used to determine η_{SC} for use in Eqs 2-4.
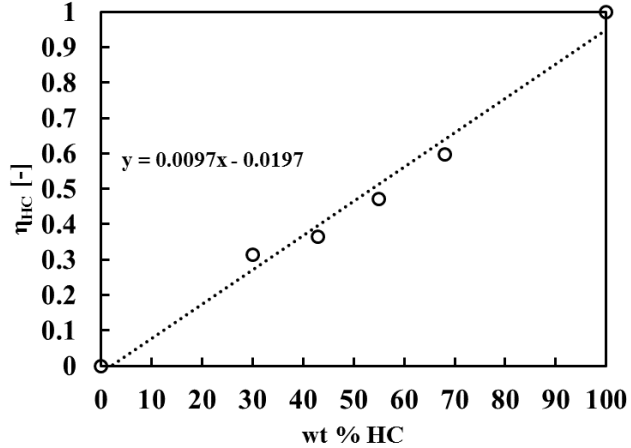

Figure 7: Volume fractions of crystalline MDI/BDO (open cyrcles) in TPUs as a function of HC concentration. The dotted line represents least squares linear fit to the above data. The equation of the linear fit is also shown.

Given the corresponding volume fractions of HC and SC, the full stiffness matrices of the 3 remaining TPU compositions (see SI) were calculated at a strain rate of $\dot{\varepsilon} = 5 \times 10^6$ s^{-1}, based on volume fractions and pure component stiffness matrices ($\mathbf{C}^{HC}$ and $\mathbf{C}^{SC}$) reported previously.[21, 22] Figure 8 shows a comparison of the composition dependence for two representative stiffnesses, C_{11} and C_{22} , with those determined directly by NEMD simulation under simple strain deformation. Stiffness increases monotonically with the wt% HC, due to the stiffer nature of crystalline MDI/BDO. The agreement between NEMD and CIM results is remarkably good, and suggests that for purposes of elastic stiffness estimation, it may be sufficient to know the elastic stiffnesses for the two pure components and their respective volume fractions; the interface itself contributes in only a minor way to the elastic response. It may be observed that the composition dependence appears to be a little stronger in the NEMD results than in CIM.
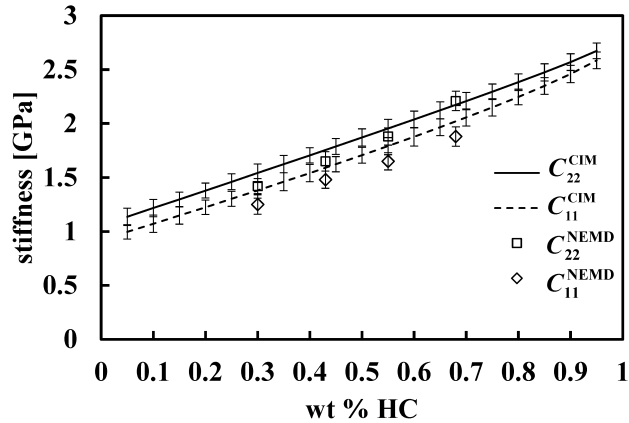
Figure 8: Stiffnesses C_{11} and C_{22} as a function of wt% HC content in TPUs. Results of NEMD simulations (open symbols); results of CIM method (lines).

Next, the orientationally averaged Voigt and Reuss limits for the Young's and shear moduli of the four TPU compositions were computed, as described in Section 2.4.3, to account for the effect of isotropically oriented lamellar stacks in TPUs. These values are shown in Figure 9(a) and 9(b), respectively. In the same figure, experimental values[87] of E and G are also shown for three TPU systems (TPU55, TPU43, and TPU30). The computed elastic moduli are significantly larger than the experimental values. Such deviation could be due to any of several reasons, including (i) approximations in the distributions of stress (equilibrium boundary conditions) and strain (traction boundary conditions) over such an aggregate of differently oriented lamellar stacks when applying CIM and Voigt or Reuss averaging, and (ii) differences in strain rate between NEMD simulation and experiment. Certain relaxation mechanisms may exist that are not operative at the fast deformation rates used in NEMD simulations, even for small deformations of the order of about 2%, but may become operative at slower deformation rates. As a consequence, the predicted response of all TPU systems to deformation would be stiffer than the corresponding experimental one. In what follows, we examine this effect of strain rate.
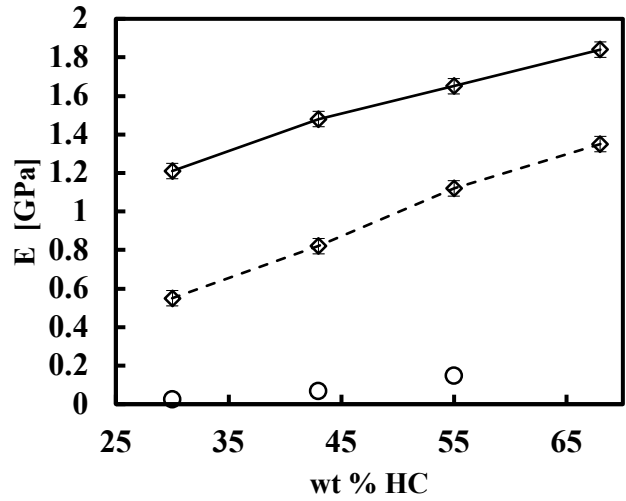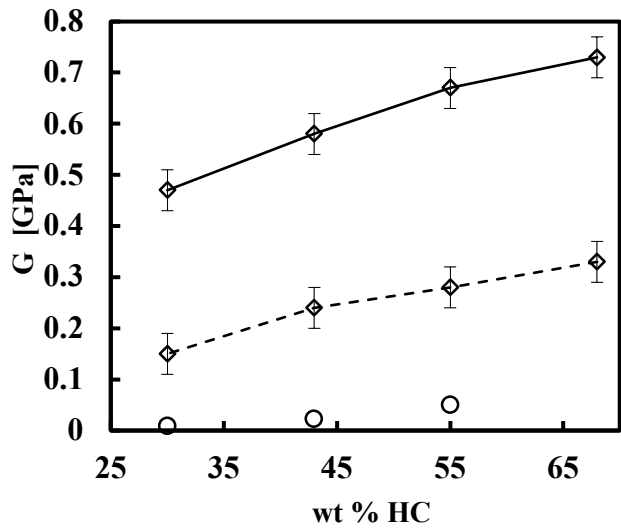
Figure 9: Spatially averaged upper (continued line) and lower (broken line) limits of a) Young's and b) shear modulus as a function of HC composition in TPUs. Experimental data[87] (O).

To illustrate this rate dependence of elastic stiffnesses, NEMD simulations for semicrystalline PTMO and crystalline MDI/BDO were run at four different deformation rates, and the resulting stiffness matrices were micromechanically homogenized via CIM and subsequently orientationally averaged. The strain rate dependence of the calculated Reuss lower bounds for the isotropically averaged moduli (at high strain rate) and the available experimental data (at low strain rate) are well described by the hyperbolic sine function (Eq 9), for the TPU

compositions for which experimental data is available.[87] Figure 10 shows the results of this analysis for the Young's modulus of TPU55, TPU43 and TPU30; the experimentally measured values for the Young's modulus and the fitting function are also shown.

The simulation and modeling results shown in Figure 10 confirm the rate dependence of Young's modulus at large deformation rates. This observation indicates that even at such large deformation rates, there were some dissipative relaxation mechanisms operative. The extrapolation of the fitting function to deformation rates comparable to the experimental ones captures more accurately the experimentally measured Young's moduli for all three TPU systems. This agreement supports the use of the hyperbolic sine function to describe the rate dependence of the elastic moduli accurately. Comparison of Young's moduli at same deformation rates among all three TPU systems (TPU55, TPU43, TPU30) shows that TPUs became stiffer (higher E) with increasing HC content.
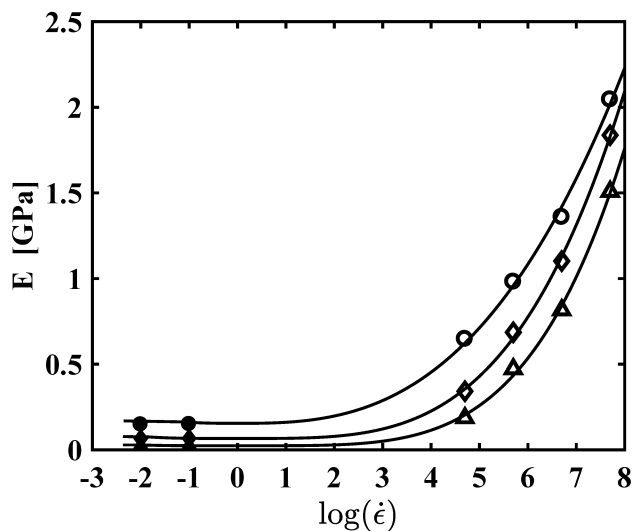
Figure 10: Rate dependence of Young's modulus for TPU55 (circles), TPU43 (diamonds), and TPU30 (triangles). Open symbols depict simulation/modeling points, filled symbols represent experimental data and the continued line illustrates the hyperbolic sine fitting function (Eq. 9).

4. Conclusions

In summary, we report the use of molecular simulations at the atomistic level to study the structure and mechanics of a common family of TPUs. For the first time, a molecular model for a

heterogeneous block copolymer, appropriately combining crystalline MDI/BDO and semicrystalline PTMO domains, was built, equilibrated and simulated in atomistic detail, using a united atom force field. With the help of the IMC algorithm, atomistic configurations of TPUs were created, and shown to sample efficiently the topological features such as bridges, loops and tails. The population distribution of these segment types in the noncrystalline region, provided estimates of the incremental chemical potential of a constituent PTMO bead and found to be in excellent agreement with previous studies on semicrystalline PTMO and polyethylene. Order parameter profiles (density ρ and orientational parameter P_2) of equilibrated TPU configurations confirmed the presence of both crystalline and amorphous domains, separated by a 1.4 nm thick interface, whose thickness was composition-independent.

The mechanical response of TPUs was evaluated in simple strain deformations using NEMD simulations. The complete stiffness tensors for four TPU compositions were evaluated in this manner. The components of the stiffness tensors were found to be dominated by the SC response when elongated perpendicular to the layer interfaces (zz strain), or sheared with shear gradient perpendicular to the layer interfaces (zx or zy shear). Elongation parallel to the interfaces (xx or yy strain) or shear deformation with gradient parallel to the interfaces (xy shear) were dominated by the HC response. The results are more or less consistent with a bilayer composite.

NEMD simulation results of semicrystalline PTMO and crystalline MDI/BDO at various strain rates were used to parametrize a micromechanical homogenization approach (CIM) with the goal to estimate the constitutive behavior of the composite TPU based on the mechanics of pure component systems. The CIM method was validated by reproducing accurately the elastic moduli extracted by NEMD calculations, and was used as a surrogate for the computationally costly NEMD simulations. By using CIM, the mechanics of TPUs with different TPU compositions was determined. Voigt and Reuss bounds for the isotropic average Young's and shear moduli were obtained for each composition by averaging over a random orientation distribution of bilayer elements. These values were found to be significantly larger than the best available experimental estimates. This deviation was attributed to the high strain rates used in the NEMD simulations. The strain rate dependence of both Young's and shear moduli was confirmed by NEMD simulations over the range of strain rates from 5×10^4 to 5×10^7 s^{-1}, and found to be well-described by a conventional hyperbolic sine function. The strain rate

26

dependence was in turn attributed to the existence of relaxation processes that become operative within this range of strain rates.

5. Acknowledgement

6. Supporting Information

Part A: Analysis of areal chain density for MDI/BDO crystal phase

Part B: Order parameter profiles for several TPU compositions

Part C: Overall stress-strain response of TPU68

Part D: Stiffness matrices for TPU55, TPU43, and TPU30

Part E: Values of Young's modulus for several TPU compositions as determined from experimental data by Cho et al.

7. References

(1)   Bayer, O.; Siefken, W.; Rinke, H.; Orthner, L.; Schild, H. A method for producing polyurethanes or polyureas [Verfahren zur Herstellung von Polyurethanen bzw. Polyharnstoffen], DE Patent 728 981, assigned to IG Farbenindustrie AG. December 7 1937.

(2)   Engels, H.-W.; Pirkl, H.-G.; Albers, R.; Albach, R. W.; Krause, J.; Hoffmann, A.; Casselmann, H.; Dormish, J. Polyurethanes: Versatile Materials and Sustainable Problem Solvers for Today's Challenges. *Angewandte Chemie International Edition* **2013,** 52, (36), 9422-9441.

(3)   Fernández d'Arlas, B.; Rueda, L.; de la Caba, K.; Mondragon, I.; Eceiza, A. Microdomain composition and properties differences of biodegradable polyurethanes based on MDI and HDI. *Polymer Engineering & Science* **2008,** 48, (3), 519-529.

(4)   Fernández-d´Arlas, B.; Rueda, L.; Fernández, R.; Khan, U.; Coleman, J. N.; Mondragon, I.; Eceiza, A. Inverting Polyurethanes Synthesis: Effects on Nano/Micro-Structure and Mechanical Properties. *Soft Materials* **2010,** 9, (1), 79-93.

(5)   Liff, S. M.; Kumar, N.; McKinley, G. H. High-performance elastomeric nanocomposites via solvent-exchange processing. *Nat Mater* **2007,** 6, (1), 76-83.

(6)   Buckley, C. P.; Prisacariu, C.; Martin, C. Elasticity and inelasticity of thermoplastic polyurethane elastomers: Sensitivity to chemical and physical structure. *Polymer* **2010,** 51, (14), 3213-3224.

(7)   Simmons, A. H.; Michal, C. A.; Jelinski, L. W. Molecular Orientation and Two-Component Nature of the Crystalline Fraction of Spider Dragline Silk. *Science* **1996,** 271, (5245), 84.

(8)   Liu, Y.; Shao, Z.; Vollrath, F. Relationships between supercontraction and mechanical properties of spider silk. *Nat Mater* **2005,** 4, (12), 901-905.

(9)   Fernández-d'Arlas, B.; Ramos, J. A.; Saralegi, A.; Corcuera, M.; Mondragon, I.; Eceiza, A. Molecular Engineering of Elastic and Strong Supertough Polyurethanes. *Macromolecules* **2012,** 45, (8), 3436-3443.

(10)   Bogoslovov, R. B.; Roland, C. M.; Gamache, R. M. Impact-induced glass transition in elastomeric coatings. *Applied Physics Letters* **2007,** 90, (22), 221910.

(11)   Grujicic, M.; Pandurangan, B.; He, T.; Cheeseman, B. A.; Yen, C. F.; Randow, C. L. Computational investigation of impact energy absorption capability of polyurea coatings via deformation-induced glass transition. *Materials Science and Engineering: A* **2010,** 527, (29–30), 7741-7751.

(12)   Xue, L.; Mock Jr, W.; Belytschko, T. Penetration of DH-36 steel plates with and without polyurea coating. *Mechanics of Materials* **2010,** 42, (11), 981-1003.

(13)   Arman, B.; Reddy, A. S.; Arya, G. Viscoelastic Properties and Shock Response of Coarse-Grained Models of Multiblock versus Diblock Copolymers: Insights into Dissipative Properties of Polyurea. *Macromolecules* **2012,** 45, (7), 3247-3255.

(14)   Rao, M. D. Recent applications of viscoelastic damping for noise control in automobiles and commercial airplanes. *Journal of Sound and Vibration* **2003,** 262, (3), 457-474.

(15)   Samali, B.; Kwok, K. C. S. Use of viscoelastic dampers in reducing wind- and earthquake-induced motion of building structures. *Engineering Structures* **1995,** 17, (9), 639-654.

(16)   Adams, R. D.; Maheri, M. R. Damping in advanced polymer–matrix composites. *Journal of Alloys and Compounds* **2003,** 355, (1–2), 126-130.

(17)   Balijepalli, S.; Rutledge, G. C. Simulation study of semi-crystalline polymer interphases. *Macromolecular Symposia* **1998,** 133, (1), 71-99.

(18)   In 't Veld, P. J.; Hütter, M.; Rutledge, G. C. Temperature-Dependent Thermal and Elastic Properties of the Interlamellar Phase of Semicrystalline Polyethylene by Molecular Simulation. *Macromolecules* **2006,** 39, (1), 439-447.

(19)   In 't Veld, P. J.; Rutledge, G. C. Temperature-Dependent Elasticity of a Semicrystalline Interphase Composed of Freely Rotating Chains. *Macromolecules* **2003,** 36, (19), 7358-7365.

(20)   Kuppa, V. K.; in 't Veld, P. J.; Rutledge, G. C. Monte Carlo Simulation of Interlamellar Isotactic Polypropylene. *Macromolecules* **2007,** 40, (14), 5187-5195.

(21)   Lempesis, N.; in 't Veld, P. J.; Rutledge, G. C. Atomistic Simulation of the Structure and Mechanics of a Semicrystalline Polyether. *Macromolecules* **2016,** 49, (15), 5714-5726.

(22)   Lempesis, N.; in 't Veld, P. J.; Rutledge, G. C. Simulation of the structure and mechanics of crystalline 4,4'-diphenylmethane diisocyanate (MDI) with n-butanediol (BDO) as chain extender. *Polymer* **2016,** 107, 233-239.

(23)   Yildirim, E.; Yurtsever, M.; Wilkes, G. L.; Yilgör, I. Effect of intersegmental interactions on the morphology of segmented polyurethanes with mixed soft segments: A coarse-grained simulation study. *Polymer* **2016,** 90, 204-214.

(24)   Yilgör, I.; Yilgör, E.; Wilkes, G. L. Critical parameters in designing segmented polyurethanes and their effect on morphology and properties: A comprehensive review. *Polymer* **2015,** 58, A1-A36.

(25)   Sami, S.; Yildirim, E.; Yurtsever, M.; Yurtsever, E.; Yilgor, E.; Yilgor, I.; Wilkes, G. L. Understanding the influence of hydrogen bonding and diisocyanate symmetry on the morphology and properties of segmented polyurethanes and polyureas: Computational and experimental study. *Polymer* **2014,** 55, (18), 4563-4576.

(26)   Briggs, J. M.; Nguyen, T. B.; Jorgensen, W. L. Monte Carlo simulations of liquid acetic acid and methyl acetate with the OPLS potential functions. *Journal of Physical Chemistry* **1991,** 95, (8), 3315-3322.

(27)   Duffy, E. M.; Kowalczyk, P. J.; Jorgensen, W. L. Do denaturants interact with aromatic hydrocarbons in water? *Journal of the American Chemical Society* **1993,** 115, (20), 9271-9275.

(28)   Jorgensen, W. L.; Briggs, J. M.; Leonor Contreras, M. Relative partition coefficients for organic solutes from fluid simulations. *Journal of Physical Chemistry* **1990,** 94, (4), 1683-1686.

(29)   Jorgensen, W. L.; Laird, E. R.; Nguyen, T. B.; Tirado-Rives, J. Monte Carlo simulations of pure liquid substituted benzenes with OPLS potential functions. *Journal of Computational Chemistry* **1993,** 14, (2), 206-215.

(30)   Jorgensen, W. L.; Madura, J. D.; Swenson, C. J. Optimized intermolecular potential functions for liquid hydrocarbons. *Journal of the American Chemical Society* **1984,** 106, (22), 6638-6646.

(31)   Jorgensen, W. L.; Maxwell, D. S.; Tirado-Rives, J. Development and testing of the OPLS all-atom force field on conformational energetics and properties of organic liquids. *Journal of the American Chemical Society* **1996,** 118, (45), 11225-11236.

(32)   Jorgensen, W. L.; Severance, D. L. Aromatic-aromatic interactions: Free energy profiles for the benzene dimer in water, chloroform, and liquid benzene. *Journal of the American Chemical Society* **1990,** 112, (12), 4768-4774.

(33)   Jorgensen, W. L.; Tirado-Rives, J. The OPLS potential functions for proteins. Energy minimizations for crystals of cyclic peptides and crambin. *Journal of the American Chemical Society* **1988,** 110, (6), 1657-1666.

(34)   Kaminski, G. A.; Friesner, R. A.; Tirado-Rives, J.; Jorgensen, W. L. Evaluation and reparametrization of the OPLS-AA force field for proteins via comparison with accurate quantum chemical calculations on peptides. *Journal of Physical Chemistry B* **2001,** 105, (28), 6474-6487.

(35)   Weiner, S. J.; Kollman, P. A.; Case, D. A.; Singh, U. C.; Alagona, G.; Profeta Jr, S.; Weiner, P.; Ghio, C. New Force Field For Molecular Mechanical Simulation Of Nucleic Acids And Proteins. *Journal of the American Chemical Society* **1984,** 106, (3), 765-784.

(36)   Jorgensen, W. L.; Swenson, C. J. Optimized intermolecular potential functions for amides and peptides. Structure and properties of liquid amides. *Journal of the American Chemical Society* **1985,** 107, (3), 569-578.

(37)   Jorgensen, W. L. Optimized intermolecular potential functions for liquid alcohols. *Journal of Physical Chemistry* **1986,** 90, (7), 1276-1284.

(38)   Jorgensen, W. L.; Briggs, J. M. Monte carlo simulations of liquid acetonitrile with a three-site model. *Molecular Physics* **1988,** 63, (4), 547-558.

(39)   Chen, B.; Potoff, J. J.; Siepmann, J. I. Monte Carlo calculations for alcohols and their mixtures with alkanes. Transferable potentials for phase equilibria. 5. United-atom description of primary, secondary, and tertiary alcohols. *Journal of Physical Chemistry B* **2001,** 105, (15), 3093-3104.

(40)   Chen, C.; Depa, P.; Sakai, V. G.; Maranas, J. K.; Lynn, J. W.; Peral, I.; Copley, J. R. D. A comparison of united atom, explicit atom, and coarse-grained simulation models for poly(ethylene oxide). *Journal of Chemical Physics* **2006,** 124, (23).

(41)   Maerzke, K. A.; Schultz, N. E.; Ross, R. B.; Siepmann, J. I. TraPPE-UA force field for acrylates and Monte Carlo simulations for their mixtures with Alkanes and alcohols. *Journal of Physical Chemistry B* **2009,** 113, (18), 6415-6425.

(42)   Stubbs, J. M.; Potoff, J. J.; Siepmann, J. I. Transferable potentials for phase equilibria. 6. United-atom description for ethers, glycols, ketones, and aldehydes. *Journal of Physical Chemistry B* **2004,** 108, (45), 17596-17605.

(43)   Wick, C. D.; Stubbs, J. M.; Rai, N.; Siepmann, J. I. Transferable potentials for phase equilibria. 7. Primary, secondary, and tertiary amines, nitroalkanes and nitrobenzene, nitriles, amides, pyridine, and pyrimidine. *Journal of Physical Chemistry B* **2005,** 109, (40), 18974-18982.

(44)   Wick, C. D.; Martin, M. G.; Siepmann, J. I. Transferable Potentials for Phase Equilibria. 4. United-Atom description of linear and branched alkenes and alkylbenzenes. *Journal of Physical Chemistry B* **2000,** 104, (33), 8008-8016.

(45)   Martí, J. Analysis of the hydrogen bonding and vibrational spectra of supercritical model water by molecular dynamics simulations. *The Journal of Chemical Physics* **1999,** 110, (14), 6876-6886.

(46)   In 't Veld, P. J. Enhanced Monte Carlo. http://montecarlo.sourceforge.net/emc/ (31-7-2016),

(47)   Balijepalli, S.; Rutledge, G. C. Conformational statistics of polymer chains in the interphase of semi-crystalline polymers. *Computational and Theoretical Polymer Science* **2000,** 10, (1–2), 103-113.

(48)   Gautam, S.; Balijepalli, S.; Rutledge, G. C. Molecular Simulations of the Interlamellar Phase in Polymers: Effect of Chain Tilt. *Macromolecules* **2000,** 33, (24), 9136-9145.

(49)   Lacks, D. J.; Rutledge, G. C. Temperature Dependence of Structural and Mechanical Properties of Isotactic Polypropylene. *Macromolecules* **1995,** 28, (4), 1115-1120.

(50)   Wilkes, C. E.; Yusek, C. S. Investigation of domain structure in urethan elastomers by X-Ray and thermal methods. *Journal of Macromolecular Science, Part B* **1973,** 7, (1), 157-175.

(51)   Dreyfuss, P., *Poly(tetrahydrofuran)*. Gordon and Breach: 1982.

(52)   Yoon, D. Y.; Flory, P. J. Chain packing at polymer interfaces. *Macromolecules* **1984,** 17, (4), 868-871.

(53)   McLean, R. S.; Sauer, B. B. Tapping-Mode AFM Studies Using Phase Detection for Resolution of Nanophases in Segmented Polyurethanes and Other Block Copolymers. *Macromolecules* **1997,** 30, (26), 8314-8317.

(54)   Furukawa, M.; Kojio, K.; Kugumiya, S.; Uchiba, Y.; Mitsui, Y. Microphase Separation of Bulk and Ultrathin Films of Polyurethane Elastomers. *Macromolecular Symposia* **2008,** 267, (1), 9-15.

(55)   Aneja, A.; Wilkes, G. L. A systematic series of 'model' PTMO based segmented polyurethanes reinvestigated using atomic force microscopy. *Polymer* **2003,** 44, (23), 7221-7228.

(56)   Choi, T.; Weksler, J.; Padsalgikar, A.; Runt, J. Influence of soft segment composition on phase-separated microstructure of polydimethylsiloxane-based segmented polyurethane copolymers. *Polymer* **2009,** 50, (10), 2320-2327.

(57)   Garrett, J. T.; Siedlecki, C. A.; Runt, J. Microdomain morphology of poly (urethane urea) multiblock copolymers. *Macromolecules* **2001,** 34, (20), 7066-7070.

(58)   Rutledge, G. C. Implications Of Metastability For The Crystal/Amorphous Interface From Molecular Simulation. *Journal of Macromolecular Science, Part B* **2002,** 41, (4-6), 909-922.

(59)   Plimpton, S. Fast Parallel Algorithms for Short-Range Molecular Dynamics. *Journal of Computational Physics* **1995,** 117, (1), 1-19.

(60)   Hoover, W. G. Canonical dynamics: Equilibrium phase-space distributions. *Physical Review A* **1985,** 31, (3), 1695-1697.

(61)   Nosé, S. A unified formulation of the constant temperature molecular dynamics methods. *The Journal of Chemical Physics* **1984,** 81, (1), 511-519.

(62)   Swope, W. C.; Andersen, H. C.; Berens, P. H.; Wilson, K. R. A computer simulation method for the calculation of equilibrium constants for the formation of physical clusters of molecules: Application to small water clusters. *The Journal of Chemical Physics* **1982,** 76, (1), 637-649.

(63)   Irving, J. H.; Kirkwood, J. G. The Statistical Mechanical Theory of Transport Processes. IV. The Equations of Hydrodynamics. *The Journal of Chemical Physics* **1950,** 18, (6), 817-829.

(64)   Voigt, W., *Lehrbuch der Kristallphysik: mit Ausschluss der Kristalloptik*. J.W. Edwards: 1928.

(65)   Arridge, R. G. C., *Mechanics of Polymers*. Clarendon Press: 1975.

(66)   Ward, I. M.; Sweeney, J., *An Introduction to the Mechanical Properties of Solid Polymers*. Wiley: 2004.

(67)   Nye, J. F., *Physical Properties of Crystals: Their Representation by Tensors and Matrices*. Clarendon Press: 1985.

(68)   Ahzi, S.; Parks, D. M.; Argon, A. S. In *Estimates of the overall elastic properties in semi-crystalline polymers*, University of California, Los Angeles, CA (United States): United States, 1995; TRN: 95:006111-0054.

(69)   Ahzi, S.; Bahlouli, N.; Makradi, A.; Belouettar, S. Composite modeling for the effective elastic properties of semicrystalline polymers. *Journal of Mechanics of Materials and Structures* **2007,** 2, (1), 1-22.

(70)   Ghazavizadeh, A.; Rutledge, G. C.; Atai, A. A.; Ahzi, S.; Rémond, Y.; Soltani, N. Micromechanical characterization of the interphase layer in semi-crystalline polyethylene. *Journal of Polymer Science Part B: Polymer Physics* **2013,** 51, (16), 1228-1243.

(71)   Ghazavizadeh, A.; Rutledge, G. C.; Atai, A. A.; Ahzi, S.; Rémond, Y.; Soltani, N. Hyperelastic characterization of the interlamellar domain and interphase layer in semicrystalline polyethylene. *Journal of Polymer Science, Part B: Polymer Physics* **2013,** 51, (23), 1692-1704.

(72)   Hori, M.; Nemat-Nasser, S. Double-inclusion model and overall moduli of multi-phase composites. *Mechanics of Materials* **1993,** 14, (3), 189-206.

(73)   Voigt, W. Ueber die Beziehung zwischen den beiden Elasticitätsconstanten isotroper Körper. *Annalen der Physik* **1889,** 274, (12), 573-587.

(74)   Reuss, A. Berechnung der Fließgrenze von Mischkristallen auf Grund der Plastizitätsbedingung für Einkristalle. *ZAMM - Journal of Applied Mathematics and Mechanics / Zeitschrift für Angewandte Mathematik und Mechanik* **1929,** 9, (1), 49-58.

(75)   Hill, R. The Elastic Behaviour of a Crystalline Aggregate. *Proceedings of the Physical Society. Section A* **1952,** 65, (5), 349.

(76)   Roetling, J. A. Yield stress behaviour of polymethylmethacrylate. *Polymer* **1965,** 6, (6), 311-317.

(77)   Richeton, J.; Ahzi, S.; Vecchio, K. S.; Jiang, F. C.; Adharapurapu, R. R. Influence of temperature and strain rate on the mechanical behavior of three amorphous polymers: Characterization and modeling of the compressive yield stress. *International Journal of Solids and Structures* **2006,** 43, (7–8), 2318-2335.

(78)   Mae, H.; Omiya, M.; Kishimoto, K. Effects of strain rate and relaxation rate on elastic modulus of semi-crystalline polymer. **2008**.

(79)   Sahputra, I. H.; Echtermeyer, A. T. Effects of temperature and strain rate on the deformation of amorphous polyethylene: a comparison between molecular dynamics simulations and experimental results. *Modelling and Simulation in Materials Science and Engineering* **2013,** 21, (6), 065016.

(80)   Blackwell, J.; Nagarajan, M. R.; Hoitink, T. B. Structure of polyurethane elastomers: effect of chain extender length on the structure of MDI/diol hard segments. *Polymer* **1982,** 23, (7), 950-956.

(81)   Born, L.; Crone, J.; Hespe, H.; Müller, E. H.; Wolf, K. H. On the structure of polyurethane hard segments based on MDI and butanediol-1,4: X-ray diffraction analysis of oriented elastomers and of single crystals of a model compound. *Journal of Polymer Science: Polymer Physics Edition* **1984,** 22, (2), 163-173.

(82)   Tsujita, Y.; Nose, T.; Hata, T. Thermodynamic Properties of Poly(ethylene glycol) and Poly(tetrahydrofuran). I. P[mdash]V[mdash]T Relations and Internal Pressure. *Polym J* **1973,** 5, (2), 201-207.

(83)   Waheed, N.; Lavine, M. S.; Rutledge, G. C. Molecular simulation of crystal growth in n-eicosane. *The Journal of Chemical Physics* **2002,** 116, (5), 2301-2309.

(84)   Stribeck, N.; Alamo, R. G.; Mandelkern, L.; Zachmann, H. G. Study of the Phase Structure of Linear Polyethylene by Means of Small-Angle X-ray Scattering and Raman Spectroscopy. *Macromolecules* **1995,** 28, (14), 5029-5036.

(85)   Strobl, G. R.; Schneider, M. Direct evaluation of the electron density correlation function of partially crystalline polymers. *Journal of Polymer Science: Polymer Physics Edition* **1980,** 18, (6), 1343-1359.

(86)   Pant, P. V. K.; Theodorou, D. N. Variable Connectivity Method for the Atomistic Monte Carlo Simulation of Polydisperse Polymer Melts. *Macromolecules* **1995,** 28, (21), 7224-7234.

(87)   Cho, H.; Pöselt, E.; Mayer, S.; Rutledge, G. C.; Boyce, M. C. Deformation Mechanisms of Thermoplastic Elastomers: Stress-Strain Behavior and Constitutive Modeling. Polymer **2017,** (submitted).